The Astrophysical Journal, 813:76 (10pp), 2015 November 1 doi:10.1088/0004-637X/813/1/76

COMPACT DUST CONCENTRATION IN THE MWC 758 PROTOPLANETARY DISK

S. Marino[1,2], S. Casassus[1,2], S. Perez[1,2], W. Lyra[3], P. E. Roman[2,4], H. Avenhaus[1,2], C. M. Wright[5], and S. T. Maddison[6]
[1] Departamento de Astronomía, Universidad de Chile, Casilla 36-D, Santiago, Chile; smarino@das.uchile.cl
[2] Millenium Nucleus "Protoplanetary Disks in ALMA Early Science," Universidad de Chile, Casilla 36-D, Santiago, Chile
[3] Department of Physics and Astronomy, California State University Northridge, 18111 Nordhoff Street, Northridge, CA 91330, USA
[4] Center of Mathematical Modeling, Universidad de Chile, Beauchef 851, Santiago, Chile
[5] School of Physical, Environmental and Mathematical Sciences, UNSW@ADFA, Canberra ACT 2600, Australia
[6] Centre for Astrophysics and Supercomputing, Swinburne University of Technology, P.O. Box 218, Hawthorn, VIC 3122, Australia
Received 2015 May 20; accepted 2015 September 30; published 2015 October 29

ABSTRACT

The formation of planetesimals requires that primordial dust grains grow from micron- to kilometer-sized bodies. Dust traps caused by gas pressure maxima have been proposed as regions where grains can concentrate and grow fast enough to form planetesimals, before radially migrating onto the star. We report new VLA Ka and Ku observations of the protoplanetary disk around the Herbig Ae/Be star MWC 758. The Ka image shows a compact emission region in the outer disk, indicating a strong concentration of big dust grains. Tracing smaller grains, archival ALMA data in band 7 continuum shows extended disk emission with an intensity maximum to the northwest of the central star, which matches the VLA clump position. The compactness of the Ka emission is expected in the context of dust trapping, as big grains are trapped more easily than smaller grains in gas pressure maxima. We develop a nonaxisymmetric parametric model inspired by a steady-state vortex solution with parameters adequately selected to reproduce the observations, including the spectral energy distribution. Finally, we compare the radio continuum with SPHERE scattered light data. The ALMA continuum spatially coincides with a spiral-like feature seen in scattered light, while the VLA clump is offset from the scattered light maximum. Moreover, the ALMA map shows a decrement that matches a region devoid of scattered polarized emission. Continuum observations at a different wavelength are necessary to conclude whether the VLA-ALMA difference is an opacity or a real dust segregation.

Key words: planet–disk interactions – protoplanetary disks – techniques: interferometric

1. INTRODUCTION

The formation of terrestial planets or of giant planets by core accretion requires the buildup of a population of planetesimals. To form these bodies, dust grains need to grow from micron to kilometer sizes, i.e., grains need to increase in size by at least nine orders of magnitude in size scale, until the influence of gravity enhances the protoplanet growth (Safronov & Zvjagina 1969; Pollack et al. 1996). This process is a race against the disk dispersal process (Hollenbach et al. 1994; Clarke et al. 2001) and accretion onto the central star (Hartmann et al. 1998).

As dust grains grow, they start to decouple from the gas and drift radially toward the central star (Weidenschilling 1977). Therefore, planetesimal formation has to happen in timescales shorter than radial drift. One way to halt the inward drift is by developing a local maximum in the radial surface density of the gas. Dust grains can easily get trapped in density maxima (Whipple 1972; Barge & Sommeria 1995; Haghighipour & Boss 2003; Chiang & Youdin 2010), especially big grains (Brauer et al. 2008; Pinilla et al. 2012). Dust traps can be found in the inner edges of disks with evidence of gaps and cavities, commonly called transitional disks (Espaillat et al. 2014). These gaps and cavities are also detected as infrared dips in the spectral energy distribution (SED). In these dust traps, and depending on the level of gas turbulence, grains can accumulate for periods comparable to the disk lifetime, thereby benefiting grain growth and producing an enhancement in the population of larger dust grains (Brauer et al. 2008; Pinilla et al. 2012).

Azimuthal asymmetries, such as vortices, can also produce dust trapping (Barge & Sommeria 1995; Tanga et al. 1996; Johansen et al. 2004; Inaba & Barge 2006; Lyra et al. 2008, 2009; Regály et al. 2012; Lyra & Lin 2013). Large-scale asymmetries are observed in submillimeter observations of the transition disks around SAO 206426, SR 21 (Pérez et al. 2014), LkHα 330 (Isella et al. 2013), and particularly in HD 142527 (Casassus et al. 2013; Fukagawa et al. 2013) and IRS 48 (van der Marel et al. 2013), where a stronger than usual azimuthal contrast is observed. These observations suggest dust trapping by large-scale vortices. In this scenario it is expected that the dust spatial distribution will depend strongly on the grain size, as aerodynamic drag depends on the grain cross section. Big grains will concentrate in more compact regions than small grains (Barge & Sommeria 1995; Klahr & Henning 1997; Dubrulle et al. 2005; Inaba & Barge 2006; Meheut et al. 2012; Lyra & Lin 2013; Raettig et al. 2015). This has strong observable implications: at long wavelengths, dust continuum emission should be more compact than at shorter wavelengths, as it traces the mass distribution of grains with sizes comparable to the observed wavelength (Beckwith et al. 1990; Testi et al. 2003; Birnstiel et al. 2013). On the other hand, Mittal & Chiang (2015) show that large and similar structures to the observed asymmetries in protoplanetary disks can be formed by gravitational global modes, which are currently difficult to discriminate from vortices. Thus, in the absence of tracers of the gas mass, it is crucial to use multiwavelength observations to diagnose whether dust trapping around a pressure maximum is present.

In this paper we study the transition disk around the Herbig Ae star MWC 758 (HD 36112). The main parameters for this system are given in Table 1. The central star is 3.7 ± 2.0 Myr old (Meeus et al. 2012), and optical spectroscopy reveals

Table 1
Main Parameters of MWC 758

Parameter	Value	References
R.A. (J2000)	$05^h\ 30^m\ 27\overset{s}{.}530$	(1)
decl. (J2000)	$+25°\ 19'\ 57\overset{''}{.}082$	(1)
Age	3.7 ± 2.0 Myr	(2)
Stellar mass	$2.0 \pm 0.2\ M_\odot$	(3)
V	8.27	(4)
$B - V$	0.3	(4)
H	6.56	(5)
Distance	279^{+94}_{-58} pc	(1)
Disk inclination	$21° \pm 2°$	(3)
Disk PA	$65° \pm 7°$	(3)

References. (1) van Leeuwen (2007); (2) Meeus et al. (2012); (3) Isella et al. (2010); (4) Høg et al. (2000); (5) Cutri et al. (2003).

variable profiles suggesting jet-like inhomogeneities at different distances from the star (Beskrovnaya et al. 1999). The revised *Hipparcos* parallax data put the star at a distance of 279^{+94}_{-58} pc (van Leeuwen 2007), although most previous studies use the old *Hipparcos* estimated distance of 200^{+60}_{-40} pc (van den Ancker et al. 1998). Studying the ^{12}CO(3-2) kinematics, Isella et al. (2010) determined a stellar mass of $2.0 \pm 0.2\ M_\odot$ and a disk orientation with an inclination (i) of $21° \pm 2°$ and a position angle (PA) of $65° \pm 7°$, all consistent with Keplerian rotation. Despite its bright infrared excess, a cavity of $0\overset{''}{.}37$ (73 astronomical units (AU) at 200 pc) has been inferred from dust millimeter emission, suggesting a depletion of millimeter grains in the inner regions of the disk possibly due to the presence of a low-mass companion within a radius of 42 AU (using the revised distance; Isella et al. 2010; Andrews et al. 2011). In addition, the SED shows a 10 μm dip consistent with a pre-transitional disk (Grady et al. 2013), but with a strong near-infrared emission coming from sub-AU scales observed with VLTI (Isella et al. 2008).

The disk structure shows deviations from an axisymmetric disk. Spiral arms are detected from near-IR scattered light and thermal emission images extending from the submillimeter cavity to the outer disk (Grady et al. 2013; Benisty et al. 2015), possibly produced by a massive planet at ~160 AU (Dong et al. 2015). The drop in the polarized intensity beyond the spiral arms can be interpreted as a shadowing effect by the arms, as the disk extends farther out in the millimeter. In addition, at millimeter wavelengths a peak intensity in the dust continuum has been detected to the northwest of the central star after subtraction of a best-fit axisymmetric model, suggesting an asymmetry in the millimeter dust grain distribution in the outer parts of the disk (Isella et al. 2010). Moreover, in the same study, asymmetries in CO emission were observed that could be due to a warped optically thick inner disk (Isella et al. 2010), similar to the case of HD 142527 (Marino et al. 2015). If the southern spiral arm is trailing, the disk is rotating with a clockwise direction in the plane of the sky, where the north side of the disk is the nearest.

We analyze new VLA Ka and Ku observations and compare with ALMA archival data to study the distribution of dust grains and search for evidence of grain size segregation due to dust trapping. In Section 2 we describe the data and imaging. In Section 3 we investigate the origin of the VLA Ka and Ku asymmetric emission, comparing with archival ALMA and SPHERE data. In Section 3.4 we describe a parametric asymmetric disk model inspired by a modified vortex solution, which can reproduce the basic morphology seen in the VLA and ALMA images and the SED, to try to interpret the observed asymmetries. In Section 4 we discuss the origin of the asymmetries: a large-scale pressure maximum, e.g., a vortex formed at the outer edge of the cavity producing dust trapping, or an embedded massive forming planet accreting material while heating its surroundings. Finally, in Section 5 we summarize the main conclusions of this work.

2. OBSERVATIONS AND IMAGING

In this section we describe the observations and imaging of the VLA Ka (~33 GHz) and Ku (~15 GHz) and ALMA Band 7 (~337 GHz) data. The image synthesis was carried out using a nonparametric least-squares modeling technique with a regularization term called entropy from the family of maximum entropy methods (MEMs). We call the whole algorithm and code *uvmem*, and the resulting deconvolved model images are labeled as the "MEM model." Examples of MEM in astronomy can be found in Pantin & Starck (1996), Casassus et al. (2006), Levanda & Leshem (2010), Casassus et al. (2013), Warmuth & Mann (2013), and Coughlan & Gabuzda (2013). It is possible to characterize the resolution level with a synthetic beam derived from the response of the algorithm to a point source with the same noise level as the observations. The MEM synthetic beam is usually finer than the standard Clean beam with natural or *briggs* weighting.

The deconvolved model images are "restored" by adding the dirty map of the residuals of uvmem and convolving with a Clean beam characteristic of natural or briggs weighting. These images can be compared with Clean images and are labeled as "restored images."

2.1. VLA

The VLA observations form part of the project VLA 13B-273. The MWC 758 observations were acquired on six runs: three nights in 2013 October and November in Ka band and another three nights in 2014 January in Ku band. In Ka band the target was observed in B 0 configuration with minimum and maximum projected baselines of 190 m and 10.5 km, while in Ku band it was observed in BnA 0 configuration with minimum and maximum projected baselines of 80 m and 23 km. The array included 27 antennas of 25 m diameter, and the total integration time on source was 1 hr, 21 minutes in each band.

For the Ka band, the VLA correlator was configured to produce 64 spectral windows from 28.976 to 37.024 GHz, with a spectral window bandwidth of 128 MHz, each divided into 64 channels to study the continuum emission with a resolution of 2 MHz. In the Ku band, the correlator was configured similarly with 64 spectral windows covering from 11.976 to 18.224 GHz, each divided into 64 channels of 2 MHz width.

In all the observations, 3c 138 was used as the primary flux calibrator, while J0547+2721 was used as the phase calibrator with four observations of 1 minute, 30 s between the target observations of 9 minutes. After looking at the resulting images from each run to check the quality of the data, we excluded one of the three observing runs with Ka band.

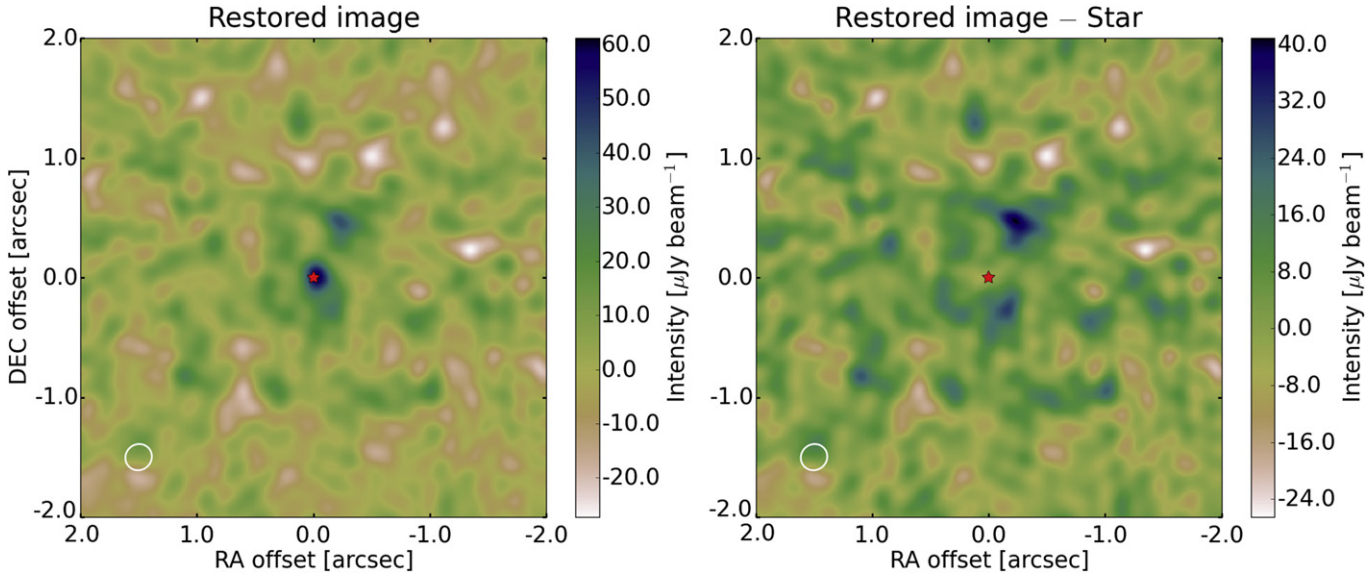

Figure 1. Restored VLA Ka (∼33 GHz) images. Left panel: restored image. Right panel: restored image after subtracting the stellar emission with a point-source fit to the visibilities. The beam size in the Ka images is $0\farcs23 \times 0\farcs22$ and is represented by a white ellipse in both images. The *x*- and *y*-axes indicate the offset from the stellar position in R.A. and decl. in arcsec, i.e., north is up and west is right. The stellar position is marked with a red star.

2.1.1. VLA Images

In Figure 1 we present the restored VLA Ka image and restored image after subtracting the central component with a point-source fit to the visibilities. The Ka image presents a noise level (σ) of 6.6 μJy beam^{-1}, and the beam size is $0\farcs23 \times 0\farcs22$ with natural weights. Two bright compact regions separated by $0\farcs5$ stand out from some extended emission, which is not very well resolved owing to low signal-to-noise ratio. The southern compact emission has a peak intensity of 63.0 μJy beam^{-1} and is located at the position where the star is expected according to the stellar coordinates and proper motion (Perryman et al. 1997). The other compact emission is 44.0 μJy beam^{-1} and is located to the northwest of the star, where Isella et al. (2010) found an intensity maximum at millimeter wavelengths. To the south of the star there is also disk emission with a peak intensity of 30.0 μJy beam^{-1}, slightly higher than 4σ. This probably corresponds to dust thermal emission from the disk and puts an upper limit to the disk emission at this frequency. However, the morphology of this emission is hard to elucidate given the noise levels and resolution. The northern clump is separated from the star by $0\farcs5$, which at a distance of ∼280 pc translates to a deprojected radius of ∼150 AU in the disk plane. The total flux at 33 GHz inside a circumference of $1\farcs0$ radius is 366 ± 49 μJy and 289 ± 33 μJy after subtracting the stellar emission.

The Ku data only show compact emission coming from the star location with a total flux of 67.1 ± 7.7 μJy and an image noise level of 4.1 μJy beam^{-1}. The synthetic beam of this observation corresponding to natural weights has a size of $0\farcs56 \times 0\farcs18$. We are not showing the Ku image because it is featureless and only shows a point source at the stellar position.

2.1.2. Flux Loss

We neglect flux loss in the VLA data. To study this possibility in the VLA Ka observations due to missing baseline spacing and limited *u*–*v* coverage, we simulate observations using the VLA Ka *u*–*v* coverage and a model image of the disk at 337 GHz (the model is described in Section 3.4). At this frequency the disk emission is more extended than at 33 GHz, and thus flux loss is more likely. We scaled the intensity levels of the model image at 337 GHz to have a simulated peak intensity equal to the Ka peak intensity. Gaussian noise was added to the model visibilities to reproduce the same noise level as the restored VLA Ka image. The final simulated image has a total flux of 620 ± 27 μJy inside a circumference of $1\farcs0$ radius, centered at the stellar position. This is consistent with the scaled model flux of 609 μJy within the estimated errors. Therefore, we conclude that there is no flux loss due to missing uv sampling in the case of the VLA data.

2.2. ALMA

To study the disk continuum emission at millimeter wavelengths, we made use of ALMA archival data in Band 7 of MWC 758 from the project 2011.0.00320.S (E. Chapillon et al. 2015, in preparation). The observations were conducted over two nights in 2012 August and October. The ALMA correlator was set in Frequency Division Mode (FDM) to provide four spectral windows divided into 384 channels, centered at 337.773 GHz with a total bandwidth of 234.363 MHz, 344.469 GHz with a total bandwidth of 234.363 MHz, 332.488 GHZ with a total bandwidth of 233.143 MHz, and 330.565 GHz with a total bandwidth of 233.143 MHz. The observations were carried out with 29 antennas of 12 m diameter. The minimum and maximum projected baselines were 15 and 375 m, respectively, and the total time on source was 12 minutes. We flagged the lines CO $J = 3$–2 (337.79599 GHz) and ^{13}CO $J = 3$–2 (330.58797 GHz) to study the dust continuum emission.

In Figure 2 we present the ALMA MEM image using uvmem and a restored image that can be compared to a Clean image. The model image has an approximate resolution of $0\farcs31 \times 0\farcs18$, derived from the response to a point source. The restored image was produced by convolving with a Clean beam of size $0\farcs64 \times 0\farcs40$ characteristic of *briggs* weighting to achieve a better resolution. In the restored image, the total flux

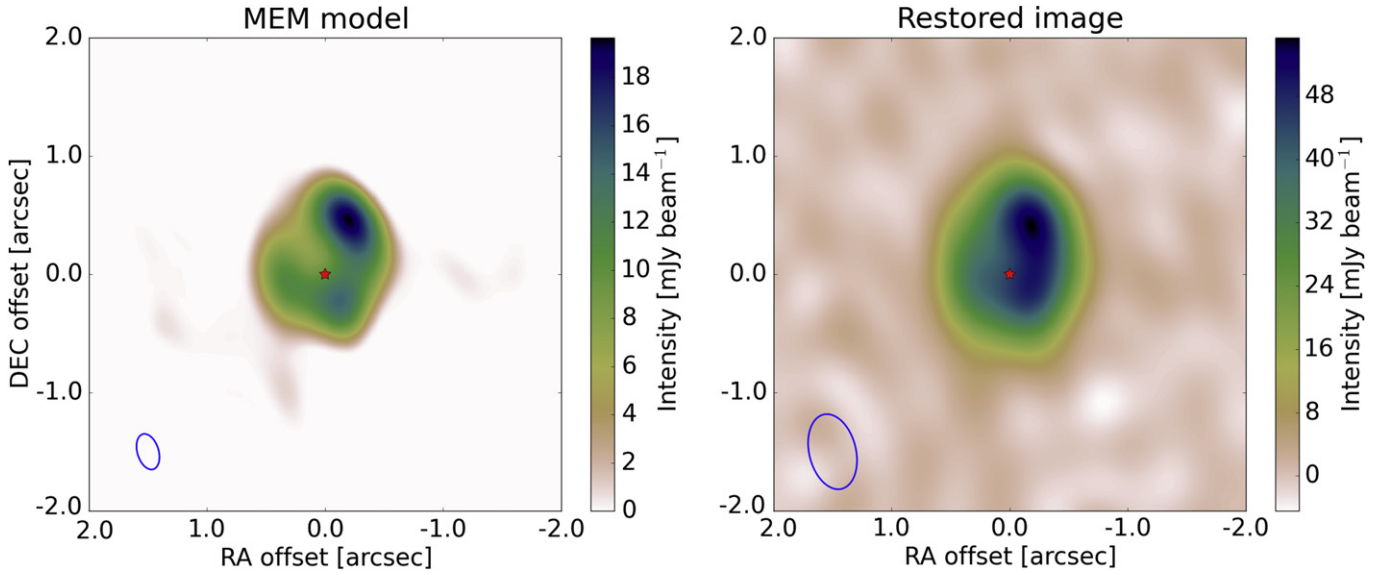

Figure 2. ALMA maps at 337 GHz (Band 7). Left panel: MEM nonparametric model (regularized with the maximum entropy method) with an approximate angular resolution of $0\farcs31 \times 0\farcs18$. Right panel: restored image adding residuals and convolving with a Clean beam corresponding to *briggs* weighting ($0\farcs64 \times 0\farcs40$). The respective beams are represented by blue ellipses. The *x*- and *y*-axes indicate the offset from the stellar position in R.A. and decl. in arcsec, i.e., north is up and west is right. The stellar position is marked with a red star.

is 210 ± 5 mJy, with a peak intensity of 55.0 mJy beam^{-1} and a noise level of 1.3 mJy beam^{-1}.

In Table 2 we summarize the new flux values of MWC 758 added by this work along with global spectral trends.

3. ANALYSIS

The VLA Ka and ALMA maps show that the disk of MWC 758 is far from an axisymmetric disk. The disk shows a peak of intensity to the northwest side of the disk, centered at a distance of $0\farcs5$ from the star, consistent with previous millimeter observations (Isella et al. 2010). In both ALMA maps and more evident in the MEM model, a local intensity minimum appears at the center of the disk, confirming the presence of a cavity of millimeter grains. Unlike the case of HD 142527 and IRS 48, the maximum and minimum of intensity are not opposite in azimuth (azimuthal wavenumber $m = 1$; Casassus et al. 2013; Fukagawa et al. 2013; van der Marel et al. 2013). Moreover, a second maximum in azimuth appears in the ALMA MEM model to the southwest of the star, which translates to an azimuthal extension to the south of the northern intensity maximum in the restored image.

3.1. Spectral Trends

To investigate the origin of the emission in the VLA maps, it is useful to compute the intra-band and inter-band spectral indexes, defined as $\alpha_{\nu_1}^{\nu_2} = \log(I_2/I_1)/\log(\nu_2/\nu_1)$. The Ka–Ku inter-band spectral index (α_{15}^{33}) of the emission coming from the stellar location is 0.36 ± 0.20, while the Ku intra-band spectral index is $\alpha_{15} = 0.8 \pm 0.6$, computed from a point-source fit to the Ku data at the different channels. Both values are consistent with free–free emission from the central star associated with a stellar wind or stellar accretion. Assuming a spectral index between 0.5 and 1.0 from free–free emission and the VLA flux level at 33 GHz, we expect emission levels of 0.2–0.7 mJy beam^{-1} at 337 GHz, well below the disk emission and the noise level reached in the ALMA data. Similar unresolved emission has been detected with ATCA observation at the location of the central star in HD 142527 with a slightly higher spectral index of 1.0 ± 0.2 (Casassus et al. 2015).

Table 2
VLA and ALMA Fluxes

Measurement	Value
ALMA Band 7 flux (337 GHz) (mJy)	205 ± 5
VLA Ka (33 GHz) flux (μJy)	366 ± 49
VLA Ka disk flux[a] (μJy)	289 ± 33
230[b]–337 GHz spectral index	3.4 ± 0.1
337–33 GHz spectral index	2.8 ± 0.1

Notes.
[a] Flux inside a circumference of $1\farcs0$ radius after subtracting the central component.
[b] Data from Chapillon et al. (2008).

On the other hand, the northern compact emission has an inter-band spectral index of $\alpha_{\rm Ka}^{B7} = 3.1 \pm 0.1$ when we compare with the intensity maximum of the restored ALMA image. Using $\alpha_{\rm Ka}^{B7}$, the predicted flux of the northern clump at 15 GHz is $\sim$6.0 μJy, slightly above the noise level of the Ku data.

Given the unknown temperatures, the uncertainties in the clump flux, the nondetection at 15 GHz, and the lack of spatial resolution in the ALMA data, it is not possible to conclude on the spectral index β for an optical depth power law $\tau(\nu) \propto \nu^{\beta}$, preventing us from studying a direct relation between the observations and a dust size distribution in the northern clump. Additional observations with similar resolution levels are necessary to derive a β index to directly study the dust size distribution in the clump. However, in Section 3.4 we implement a simple parametric vortex model for the disk that reproduces the SED and morphology of the VLA and ALMA maps. We use this model to interpret the VLA clump in Section 3.4.

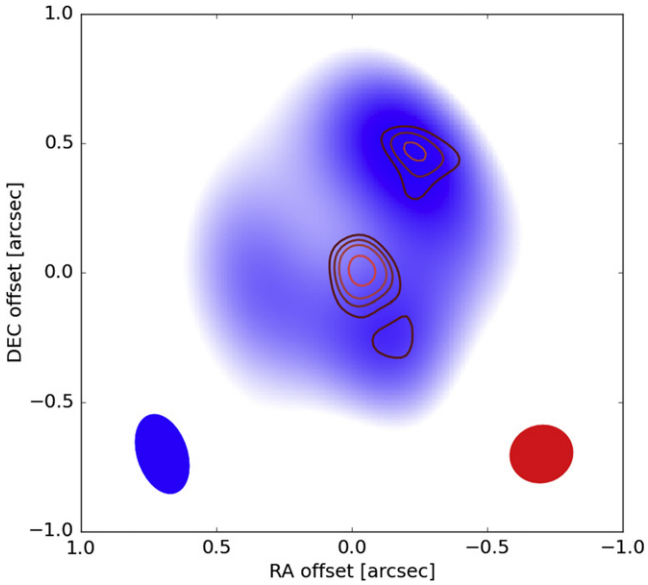

Figure 3. ALMA–VLA overlay. In blue is the ALMA Band 7 MEM model in an arbitrary color scale, while in red is the restored VLA Ka image contours set at arbitrary levels to highlight the morphology (the lowest contour level is 4.2σ). The beam size of the restored VLA Ka image and ALMA MEM model is represented by a red and blue ellipse, respectively. The *x*- and *y*-axes indicate the offset from the stellar position in R.A. and decl. in arcsec, i.e., north is up and west is right.

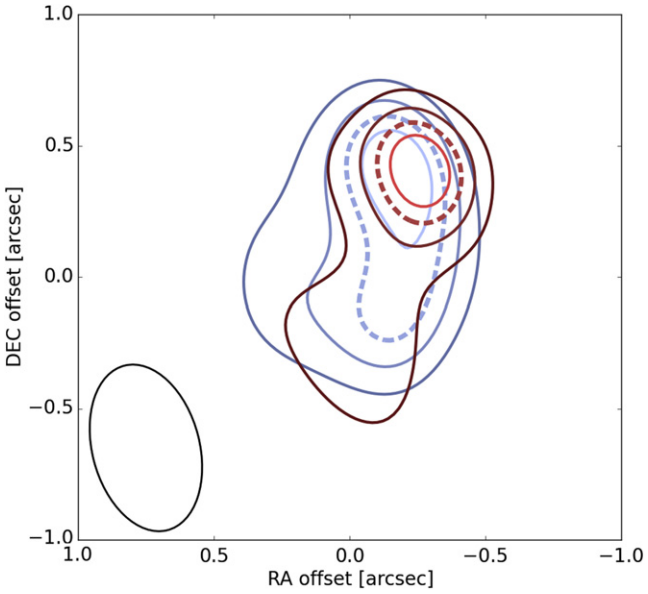

Figure 4. ALMA–VLA map contour overlay. Blue contours: ALMA Band 7 restored image. Red contours: degraded VLA image (restored image after subtracting the star and convolving with the ALMA beam). The contour levels are 0.6, 0.75, 0.85, and 0.92 times the peak intensity of each map. The lowest contour level of the VLA map represents $\sim 3\sigma$ at this resolution. The dashed red and blue lines represent the 0.85 peak intensity level. The beam size of both maps is represented by a black ellipse. The *x*- and *y*-axes indicate the offset from the stellar position in R.A. and decl. in arcsec, i.e., north is up and west is right.

3.2. Comparison between ALMA and VLA Ka Maps

In Figure 3 we present an overlay between the restored VLA Ka image and the ALMA Band 7 MEM model. The VLA Ka northern peak intensity matches the location of the ALMA Band 7 maximum. At 337 GHz we expect that most of the emission comes from ∼millimeter-sized grains. If this intensity maximum is tracing a maximum in the dust density distribution of millimeter-sized grains, the VLA and ALMA maximum could be due to dust grains being trapped in a pressure maximum of the gas. In the dust trap scenario, we would expect to observe at centimeter wavelengths a higher contrast between the intensity maximum and the rest of the disk and a more compact emission, probing the distribution of centimeter-sized grains that are more easily trapped in gas pressure maxima. However, the ALMA maps are not as well spatially resolved as the VLA Ka image owing to differences in the *u*–*v* coverage. In Section 3.3 we compare both data sets at the same resolution level.

Figure 3 also shows disk emission to the south of the stellar position in the VLA Ka map that matches a second peak intensity in the ALMA MEM model. This peak is closer in than the northern clump, at an angular distance of $\sim 0\farcs3$. However, this local maximum disappears in the restored ALMA image owing to the larger beam.

3.3. ALMA and VLA Ka Map at the Same Resolution Level

To bring both data sets to comparable resolutions, we convolved the restored VLA Ka image with the ALMA Clean synthetic beam of size $0\farcs64 \times 0\farcs40$ after subtracting the stellar emission. We call this map the degraded VLA image. In Figure 4 we show the contour levels 0.6, 0.75, 0.85, and 0.92 times the peak intensity of the degraded VLA and restored ALMA images. The degraded VLA image presents a morphology similar to the ALMA MEM model with two peak intensities: to the northwest and south of the star (see Figure 2). The northern clump in the degraded VLA image is still more compact than in the restored ALMA image, with a larger contrast. The solid angle inside the 0.85 intensity maximum contour in the degraded VLA image is 0.09 arcsec^2, while it is 0.23 arcsec^2 in the ALMA map. This result supports the dust trap interpretation, finding that the 33 GHz dust emission is more compact than at 337 GHz.

The peak intensity to the south of the star in the restored VLA Ka image remains after star subtraction and convolution with the ALMA beam, with a morphology similar to that observed in the ALMA MEM model. The nature of this compact emission is not clear as it is just ∼4 times the noise level in the restored VLA Ka image. At the ALMA resolution the cavity is hard to distinguish, although the peak intensity is offset from the stellar position in both maps, suggesting a cavity depleted of big grains.

To confirm the dust trap interpretation, ALMA observations in extended configuration are required to resolve the disk with a similar or finer resolution than the VLA Ka observations. Deeper VLA observations are also necessary to detect the rest of the disk.

3.4. Parametric Nonaxisymmetric Model

We develop a parametric nonaxisymmetric disk model, inspired by the steady-state vortex solution to the gas and dust distribution described in Lyra & Lin (2013, hereafter LL13). The aim is to reproduce part of the morphology seen in the ALMA and VLA maps and the global SED. The model consists of a central star surrounded by a disk of gas and dust. We model the star using a Kurucz template spectrum (Castelli 1993) with a temperature of 8250 K and a stellar radius of

Table 3
Disk Parameters

Parameter	Inner Disk	Outer Disk
$r_{\rm min}$ (AU)	0.2	20.0
$r_{\rm max}$ (AU)	80.0	300.0
$\Sigma(r)$	$\Sigma_c\left(\frac{r}{r_c}\right)^{-0.5}$	Equation (6)
$H(r)$ (AU)	$0.2\left(\frac{r}{1.0\ \rm AU}\right)^{1.1}$	$19.0\left(\frac{r}{100.0\ \rm AU}\right)$
M_d[a] ($M_\odot$)	5.0×10^{-8}	7.1×10^{4}
Mass fraction in Silicates	0.9	0.48
$a_{\rm min}$ (μ)	0.1	1.0
$a_{\rm max}$ (μ)	1.0	4×10^{3}

Note.
[a] The dust size distribution is $n(a)\propto a^{-3.5}$. The dust internal density for silicate and amorphous carbon grains is 4.0 and 2.0 g cm^{-3}, respectively.

$2.6\,R_\odot$, to fit the SED in the optical with a visual extinction of 0.22 (van den Ancker et al. 1998). We define two distinct disk zones (see Table 3).

1. A dusty inner disk with small grain sizes ranging from 0.1 to 1 μm, composed of amorphous carbon and silicate grains to reproduce the NIR excess.
2. A nonaxisymmetric outer disk composed of amorphous carbon and silicate grains to reproduce part of the disk morphology seen in the VLA and ALMA images, and the photometry from the SED in the FIR and radio.

The total gas mass in the disk is $0.1\,M_*$. The outer disk incorporates an analytic prescription for a steady-state vortex defined for both gas and dust distribution, based on the work of LL13. We first define an axisymmetric gas background inspired by the surface density distribution used in Isella et al. (2010), and following the solution for the surface density of a viscous Keplerian disk (Lynden-Bell & Pringle 1974)

$$\Sigma_b(r)=\Sigma_c\left(\frac{r}{r_c}\right)^{-\gamma}\exp\left(-\frac{1}{2(2-\gamma)}\left[\left(\frac{r}{r_c}\right)^{2-\gamma}-1\right]\right), \quad (1)$$

$$\rho_b(r,z,S)=\frac{\Sigma_b(r)\sqrt{S+1}}{\sqrt{2\pi}H}\exp\left[-\frac{z^2}{2H^2}(S+1)\right], \quad (2)$$

where H is the scale height of the disk and S is defined as the ratio between the the Stokes number (St) and δ_t, a turbulent diffusion parameter that measures the strength of the turbulence in the disk. We assume a global δ_t in the disk for simplicity, although the turbulence in the core of the vortex can be driven by different mechanisms than in the rest of the disk. We set $r_c=120.0$ AU and $\gamma=-2.0$ to form an outer disk that matches the peak intensity and cavity in the ALMA observations and the SED at long wavelengths, similar to the profile derived in Isella et al. (2010). However, these parameters are not well constrained owing to the lack of spatial resolution in the ALMA data and SED degeneracies.

We add the vortex steady-state solution described by Equation (64) in LL13 with a slight modification to include a global disk gas density field. We impose that the gas density described by the vortex solution has to match the gas background at the vortex boundary where the vortex flow becomes supersonic with respect to the disk. This happens when a (defined in LL13 as the axial elliptical coordinate corresponding to the vortex's semiminor axis) is equal to $\frac{H}{\chi\omega_V}$, where χ is the vortex aspect ratio and $\omega_V=\Omega_V/\Omega$ is the dimensionless vortex frequency. The same applies to the dust, and a general equation for both gas and dust can be written as

$$\rho(r,\phi,z)=\rho_b(r,z)\max\left\{1,\,c\,\rho_V(r,\phi)\right\}, \quad (3)$$

$$\rho_V=\exp\left[-\left(\frac{(r-r_0)^2}{2H_v^2}+\frac{r_0^2\phi^2}{2H_v^2\chi^2}\right)\right], \quad (4)$$

$$c=\exp\left[\frac{f^2(\chi)}{2\chi^2\omega_v}(S+1)\right], \quad (5)$$

where c is the contrast between the density maximum inside the vortex and the background density field ρ_b at the same radius (see Appendix A for more details). Here c is defined to have a global density field that matches the background density field at the vortex boundary. $H_v=H/(f(\chi)\sqrt{S+1})$ is the vortex scale length, where $f(\chi)$ is a scale function defined in LL13 and is a function of χ. A smooth solution for the density field, considering a smooth shock perimeter, can be written as

$$\rho(r,\phi,z,S)=\rho_b(r,z)\left[1+(c-1)\rho_V(r,\phi,z,S)\right]. \quad (6)$$

We set $\chi=5$ (which is not well constrained, but between the range of accepted values to remove the elliptical instability at the vortex center; Lesur & Papaloizou 2009) and $\delta_t=3\times10^{-3}$. To compute ω_V, we use the Goodman–Narayan–Goldreich solution (Goodman et al. 1987).

Using Equation (3) and reasonable values for $\delta_t=10^{-2}$–10^{-3}, it is impossible to produce a vortex with the contrast required to reproduce the asymmetry seen in the ALMA maps. To increase the contrast with the disk background, we artificially extend the vortex steady-state solution beyond its original boundary to obtain a better match with the observations (see Section 4 for a discussion on this). This translates into changing c to $\exp\left[r_s^2\frac{f^2(\chi)}{2\chi^2\omega_v}(S+1)\right]$, where r_s is the ratio between the increased vortex size and the vortex original boundary (see Appendix A for a detailed description). We set $r_s=3$ to have a good match between the restored ALMA image and the model image convolved with the synthetic ALMA beam (see Figures 2 and 5(d)).

We implement the model using nine dust species in total: two dust species for the inner disk, representing silicates and amorphous carbon grains, and seven dust species for the outer disk, one accounting for small amorphous carbon grains (from 1 to 10 μm), while the rest represent silicate grains from 1 μm to 4 mm with different spatial distributions set by Equation (6). The opacities for each dust species in the model are computed using the "Mie Theory" code written by Bohren & Huffman (1983) considering a dust size distribution with a power-law index of -3.5 and optical constants for amorphous carbon (Li & Greenberg 1997) and "Astronomical silicate" (Draine 2003). The emergent intensities from our model at different frequencies were computed using RADMC-3D version[7] 0.39 (Dullemond et al. 2015), using the Henyey & Greenstein (1941) parameterization of the phase function of scattering.

In Figure 5 we present the model images at 33 and 337 GHz at the top. The middle panels show the simulated observations

[7] http://www.ita.uni-heidelberg.de/~dullemond/software/radmc-3d/

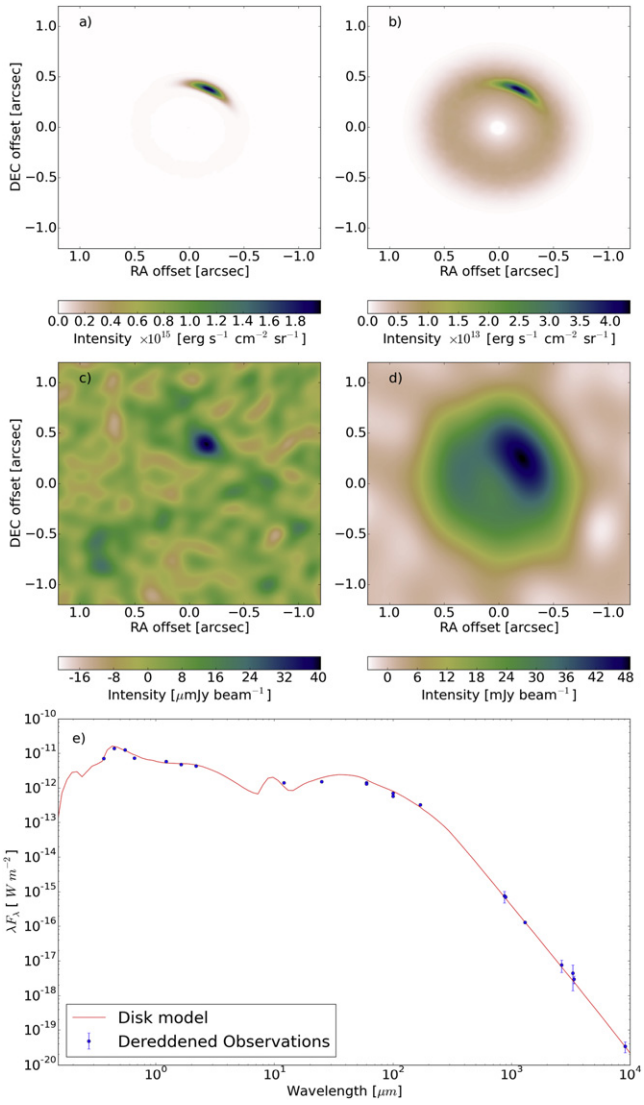

Figure 5. Parametric model predictions. (a) 33 GHz model image. (b) 337 GHz model image. (c) Simulated VLA Ka observation using the model image. (d) Simulated ALMA Band 7 observation using the model image. (e) Dereddened SED of MWC 758 (blue dots) compared with the model (red line). Photometric data points were taken from Høg et al. (2000), Cutri et al. (2003), Elia et al. (2005), Chapillon et al. (2008), Isella et al. (2010), and the new VLA Ka and archival ALMA Band 7 data presented in this work. We deredden the observations assuming a visual extinction $A_V = 0.22$ (van den Ancker et al. 1998) and a total-to-selective extinction ratio of $R_V = 3.1$. The error bars represent 2σ errors. In (a)–(d) the x- and y-axes indicate the offset from the stellar position in R.A. and decl. in arcsec, i.e., north is up and west is right.

of the model images with the same u–v coverage and noise levels of the VLA Ka and ALMA observations. In addition, we present the model SED that matches roughly the observations. As expected from the vortex model, at long wavelengths the disk emission is concentrated in the pressure maximum as it traces the distributions of bigger grains that are highly trapped inside the vortex.

The simulated ALMA image shows a peak of intensity similar to the restored ALMA image, although the morphology is not exactly the same. An interesting difference is the second intensity maximum seen in the ALMA MEM image, which appears as an extension to the south of the maximum in the restored image. This cannot be reproduced by a single and unresolved density maximum, as our model shows. A second

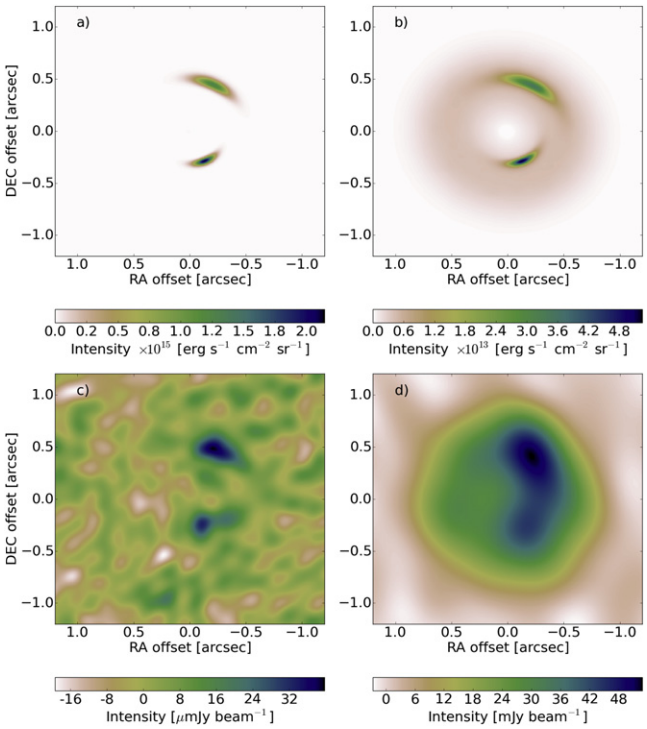

Figure 6. Parametric model predictions with two vortices. (a) 33 GHz model image. (b) 337 GHz model image. (c) Simulated VLA Ka observation using the model image. (d) Simulated ALMA Band 7 observation using the model image. In (a)–(d) the x- and y-axes indicate the offset from the stellar position in R.A. and decl. in arcsec, i.e., north is up and west is right.

vortex would be needed to account for this emission. In Figure 6 we present the model predictions and simulated observations of a model with two vortices located at the position of the VLA northern and southern clumps. The southern extension of the ALMA peak intensity is naturally reproduced, and also a decrement appears at the northeast side of the disk owing to the elongated beam (see figure in Appendix B). The VLA simulated observations show two unresolved clumps at the location of the VLA northern and southern clumps. The disk parameters are the same as the ones described above. The second vortex is located at a radius of 90 AU, and it has a size ratio r_s of 3.12.

If the northern clump emission seen in MWC 758 in Band 7 and Ka data is produced by a dust trap, it is a possible location for planetesimal and planetary core formation, as grains can grow faster and avoid the inward drift. From our model the dust temperature at the clump position is ∼30 K, but in the observations the brightness temperature of the clump at 33 GHz is 1.0 K. Thus, it is highly unresolved or it is optically thin at this frequency. From our synthetic model, the inferred dust mass inside the vortex boundary is $\sim 45\ M_\oplus$, enough mass to form several planetesimals that could lead to the formation of a planetary core of a gas giant. However, grain porosity is not included in our model; thus, this inferred mass is probably higher than the real value.

3.5. Comparison with SPHERE PDI Data

We also compare the VLA and ALMA observations with publicly available VLT SPHERE/IRDIS PDI (polarimetric differential imaging) data (Benisty et al. 2015). The data were taken on 2014 December 5 during the science verification time

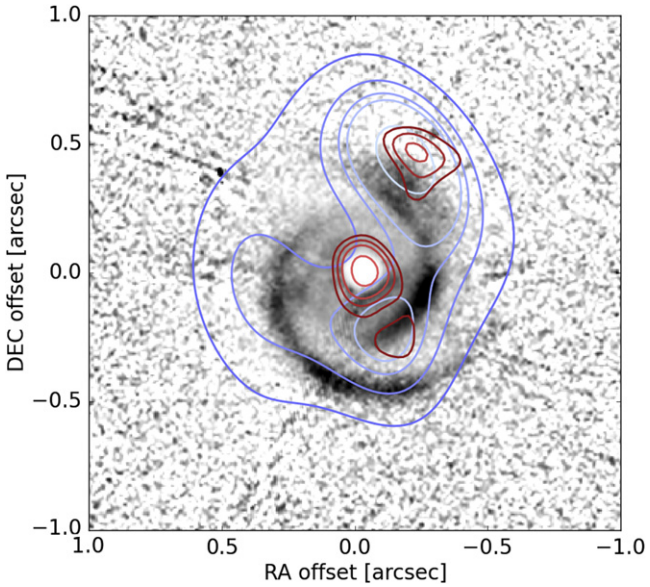

Figure 7. SPHERE/IRDIS-ALMA–VLA overlay. In grayscale is the polarized intensity scaled by r^2 to highlight the surface density of the disk, obtained with SPHERE/IRDIS PDI. The decrement in the center corresponds to the position of the coronagraph. The ALMA Band 7 MEM map is presented in blue contours, while the restored VLA Ka map is presented in red contours. The contour levels are arbitrary to emphasize the disk morphology. The *x*- and *y*-axes indicate the offset from the stellar position in the R.A. and decl. in arcsec, i.e., north is up and west is right.

of SPHERE. MWC 758 was observed in DPI (dual polarimetric imaging) mode in *Y* band (1.04 μm) with the IRDIS subinstrument of SPHERE, with a 185 mas diameter coronagraphic mask and a Lyot apodizer. Seventy exposures of 64 s each were taken, of which 48 (total integration time 51.2 minutes) were used for the reduction presented in this paper. PDI has proven to be a powerful technique to suppress the stellar light, and to first order it approximates the reflected light off the disk surface by only measuring the polarized fraction of the light (Avenhaus et al. 2014). The frames were dark-subtracted and flat-fielded, and bad pixels were removed and then centered. The polarized flux was calculated and instrumental effects accounted for in a way similar to that described in the Appendix of Avenhaus et al. (2014). In Figure 7, the resulting SPHERE image reveals the disk outside of the inner working angle set by the coronagraph, including a strong, two-armed spiral.

Unlike the case of HD 142527, where a large cavity of ~130 AU is seen in scattered light (Avenhaus et al. 2014) and in the submillimeter (Casassus et al. 2013; Fukagawa et al. 2013), exposing the inner rim of the outer disk to stellar radiation, the SPHERE PDI *Y*-band image of MWC 758 shows that, down to the inner working angle (26 AU), the cavity is not depleted of micron-sized dust grains traced at this wavelength. Moreover, the polarized surface brightness drops abruptly behind the spiral arms, as if the arms shadowed the outer disk (Grady et al. 2013). The presence of micron-sized dust grains could be linked to flaring of the gas disk, the mass of a possible gap-opening planet (Fouchet et al. 2010), or we might be looking at different stages of similar systems.

In the same figure, contours from the ALMA Band 7 MEM and restored VLA Ka image are overplotted in blue and red, respectively. No evident correlation appears between the most southern spiral arm and the dust emission at 337 and 33 GHz, although we lack spatial resolution in the ALMA data to trace fine structures. On the other hand, the disk emission to the south of the star in the ALMA and VLA maps matches part of the western arm, while the VLA northern clump maximum is slightly offset (~0.″2) from the SPHERE PDI maximum at the same PA. Such a radial displacement could be explained if there were a large wall of dust with a higher scale height shadowing the disk at the clump radius. This is probably related to a moderate or low flaring in the outer disk.

The SPHERE image also shows a region devoid of scattered light emission to the northeast between two bright arms, matching also a decrement in the ALMA MEM model that extends from the outer disk to the stellar position. The origin of this decrement could be related to a shadowing effect rather than a lack of material.

4. DISCUSSION

MWC 758 shows spiral arms, nonaxisymmetric dust thermal emission, and asymmetries in the CO emission. The origin of all the disk asymmetries is hard to elucidate. A possible explanation for the nonaxisymmetric disk seen at millimeter wavelength is a dust trap caused by a pressure maximum. A steady-state vortex as the one proposed in LL13 cannot produce such a high contrast between the dust density in the vortex core and the disk background. A solution could be linked to the vortex tail, which also causes dust trapping and can extend farther out from the vortex core (Lesur & Papaloizou 2009, 2010; Railton & Papaloizou 2014). Recently, Surville & Barge (2015) showed that vortices larger than the scale height might exist. Moreover, numerical MHD simulations have shown that high contrasts in the gas density field can be reached when large vortices form at the edge of planet-induced gaps, surviving for ~1000 orbits (Zhu & Stone 2014).

On the other hand, the azimuthal dust density structure in the outer disk is probably more complex than an azimuthal wavenumber $m = 1$. The second intensity maximum in the ALMA MEM model could be related to a second vortex at the inner edge of the outer disk. MHD simulations predict multiple vortices to form by the Rossby Wave Instability at the inner edges of "dead zones" (Lyra & Mac Low 2012). Moreover, the decrement to the northeast in the ALMA and SPHERE images cannot be easily explained by a decrement in the dust density and a single density maximum.

An alternative explanation to the asymmetry in the dust continuum emission at 337 GHz is that there is a strong asymmetry in the dust temperature field in the outer disk, similar to HD 142527, where a large crescent shows two peak intensities separated by a decrement in temperature caused by shadows cast by a tilted inner disk (Casassus et al. 2015; Marino et al. 2015). If the possible decrement in MWC 758 is produced by a tilted or warped inner disk, we would expect to see clear decrements almost opposite in azimuth, similar to the decrements in HD 142527 seen in polarized light (Avenhaus et al. 2014). Another possibility is that the spiral arms seen in scattered light (Grady et al. 2013; Benisty et al. 2015) cast shadows in the outer disk at different azimuth and radii. Moreover, a combination of both scenarios could be present. This could explain the asymmetric CO emission (Isella et al. 2010) as a temperature effect, the formation of spiral arms due to tidal forces from an inclined inner disk, or produced as a dynamic consequence of a perturbation of the gas temperature field (M. Montesinos et al. 2015, in preparation). However, the

compact emission to the northwest of the star at centimeter wavelengths seen in the VLA maps suggests that the dust concentration is real, although azimuthal structure in the dust temperature field is expected as the disk is not axisymmetric.

The compact emission in the VLA Ka data could also be explained by a companion object, e.g., a forming planet accreting material. This planet could also be responsible for the observed spiral arms in scattered light, as it is close to the planet proposed by Dong et al. (2015). Such a forming planet would have higher temperatures than a passive disk as it is accreting, also heating the disk around it. ALMA multiband continuum and gas line observations would be ideal to disentangle whether the VLA and ALMA Band 7 asymmetries are density or temperature effects and whether the VLA clump is accreting or not. Additional Hα high-contrast imaging could reveal the presence of an accreting companion.

5. CONCLUSIONS

We report new VLA observations at 33 and 15 GHz observations of the disk around the star MWC 758. The disk emission at these wavelengths traces the distribution of centimeter-sized dust grains. We found a compact disk emission at the same location where previous SMA and CARMA observations found deviations from an axisymmetric model at shorter wavelengths (Isella et al. 2010). This compact emission is at $0\farcs5$ ($\sim$150 AU) from the central star.

The VLA data also show a strong compact emission coming from the star position, characterized by a spectral index of $\sim$0.5. This is likely due to free–free emission from the central star associated with a stellar wind or stellar accretion.

We compare these data with ALMA archival data, producing ALMA Band 7 continuum deconvolved and restored images with a finer resolution than previous SMA and CARMA observations. Both maps show nonaxisymmetric disk emission, with a peak intensity at the same location as the VLA clump, but more extended. These multiwavelength observations fit in the context of dust trapping, as the bigger grains traced at lower frequencies are more concentrated around pressure maxima than the ALMA emission around the maximum. However, in the ALMA maps the disk is not as resolved as in the VLA data. New ALMA long-baseline observations are needed to resolve better the disk morphology at millimeter wavelengths and to confirm the dust trapping effect.

In addition, we compare these observations with a new reduction of archival VLT SPHERE PDI images. There is an offset of $\sim0\farcs2$ between the VLA clump and the northwestern spiral feature. The same arm matches a second intensity maximum in the dust continuum seen in the VLA and ALMA maps. More interestingly, the decrement to the northeast in the ALMA MEM model matches a decrement in the polarized intensity, suggesting a shadowing effect rather than lack of material.

We develop a parametric nonaxisymmetric model for the disk, incorporating a steady-state vortex solution based on LL13. Such a vortex model cannot explain the decrement seen to the northeast of the star and a second maximum seen in the VLA and ALMA data. To reproduce the peak intensity of the ALMA image, we are required to extend the vortex solution artificially beyond the shock perimeter. We also find that a second vortex could explain the extension to the south of the ALMA peak intensity and the decrement to the northeast as an image reconstruction artifact.

MWC 758 is a very complex protoplanetary disk, and there are still details to be addressed: what is the link between the possible vortex or vortices and the spiral arms and apparent decrements? The missing piece of the puzzle might be found with a detailed study of the disk kinematics.

S.M., S.C., S.P., and H.A. acknowledge support from the Millennium Science Initiative (Chilean Ministry of Economy), through grant "Nucleus P10-022-F." S.M. acknowledges CONICYT-PCHA/MagisterNacional/2014—folio 22140628. S.C., S.P., and H.A. acknowledge financial support from FONDECYT grants 1130949, 3140601, and 3150643, respectively. P.E.R. thanks the Chilean Postdoctoral Fondecyt project number 3140634 and ALMA-Conicyt project number 31120006. C.M.W. acknowledges support from ARC Future Fellowship FT100100495. S.T.M. acknowledges the support of the visiting professorship scheme from Université Claude Bernard Lyon 1.

This paper makes use of the following ALMA data: ADS/JAO.ALMA#2011.0.00320.S. ALMA is a partnership of ESO (representing its member states), NSF (USA), and NINS (Japan), together with NRC (Canada) and NSC and ASIAA (Taiwan) and KASI (Republic of Korea), in cooperation with the Republic of Chile. The Joint ALMA Observatory is operated by ESO, AUI/NRAO, and NAOJ.

APPENDIX A
VORTEX MODEL

Following the procedure of LL13, to match the the vortex steady-state solution from LL13 with a gas density background, we impose both density profiles to match at the vortex boundary where the vortex flow becomes supersonic. This happens when a (defined in LL13 as the axial elliptical coordinate corresponding to the vortex's semiminor axis) is equal to $\frac{H}{\chi\omega_V}$, where χ is the vortex aspect ratio and $\omega_V = \Omega_V/\Omega$ is the dimensionless vortex frequency. Assuming that the vertical dependence is the same inside and outside the vortex, we can focus only on the midplane. The density field inside the vortex can be written as

$$\rho(a, S) = c\rho_b \exp\left[-\frac{a^2 f^2(\chi)}{2H^2}(S+1)\right], \tag{7}$$

where c is a constant that has to be determined imposing the following condition:

$$\rho_b = \rho\left(a = \frac{H}{\chi\omega_V}, S\right), \tag{8}$$

$$\rho_b = c\rho_b \exp\left[-\frac{f^2(\chi)}{\chi^2\omega_V^2}(S+1)\right], \tag{9}$$

finally obtaining $c = \exp\left[\frac{f^2(\chi)}{\chi^2\omega_V^2}(S+1)\right]$. Thus, the global solution is

$$\rho(r, \phi, z) = \rho_b(r, z)\max\left\{1, c\,\exp\left[-\frac{a^2 f^2(\chi)}{2H^2}(S+1)\right]\right\}. \tag{10}$$

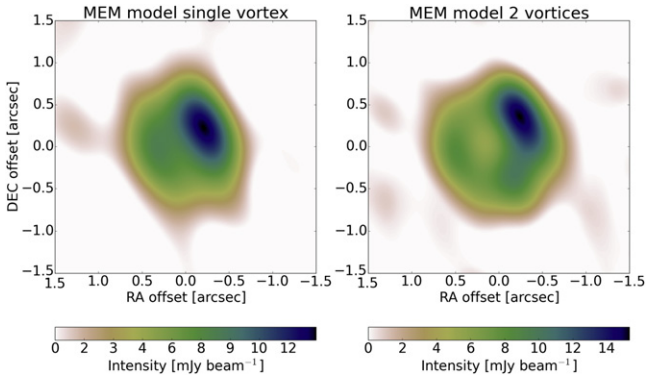

Figure 8. MEM nonparametric models (regularized with the maximum entropy method) obtained from simulated observations at 337 GHz using the disk model described in Section 3.4. The left panel shows the deconvolved image of a disk model with a single vortex, while the right panel shows the deconvolved image of a disk model with two vortices. The resolution of these observations is approximated by a beam of $0\farcs31 \times 0\farcs18$. The *x*- and *y*-axes indicate the offset from the stellar position in R.A. and decl. in arcsec, i.e., north is up and west is right. The stellar position is marked with a red star.

A more realistic or smoother solution can be written as

$$\rho(r, \phi, z) = \rho_b(r, z)\left(1 + (c - 1)\exp\left[-\frac{a^2 f^2(\chi)}{2H^2}(S + 1)\right]\right). \quad (11)$$

If we extend the vortex from its original boundary to $\frac{r_s H}{\chi \omega_V}$, c has to be redefined as $c = \exp\left[\frac{r_S^2 f^2(\chi)}{\chi^2 \omega_V^2}(S + 1)\right]$, and the final density field is described by Equation (11).

APPENDIX B
MEM VORTEX MODEL

Figure 8 shows the MEM models of the ALMA-simulated observations with a single and two vortices.

REFERENCES

Andrews, S. M., Wilner, D. J., Espaillat, C., et al. 2011, ApJ, 732, 42
Avenhaus, H., Quanz, S. P., Schmid, H. M., et al. 2014, ApJ, 781, 87
Barge, P., & Sommeria, J. 1995, A&A, 295, L1
Beckwith, S. V. W., Sargent, A. I., Chini, R. S., & Guesten, R. 1990, AJ, 99, 924
Benisty, M., Juhasz, A., Boccaletti, A., et al. 2015, A&A, 578, L6
Beskrovnaya, N. G., Pogodin, M. A., Miroshnichenko, A. S., et al. 1999, A&A, 343, 163
Birnstiel, T., Dullemond, C. P., & Pinilla, P. 2013, A&A, 550, L8
Bohren, C. F., & Huffman, D. 1983, Absorption and Scattering of Light by Small Particles (New York: Wiley)
Brauer, F., Dullemond, C. P., & Henning, T. 2008, A&A, 480, 859
Casassus, S., Cabrera, G. F., Förster, F., et al. 2006, ApJ, 639, 951
Casassus, S., van der Plas, G., Perez, S. M., et al. 2013, Natur, 493, 191
Casassus, S., Wright, C., Marino, S., et al. 2015, ApJ, 812, 126
Castelli, F. 1993, ATLAS9 Stellar Atmosphere Programs and 2 Km/s grid (Cambridge, MA: SAO)
Chapillon, E., Guilloteau, S., Dutrey, A., & Piétu, V. 2008, A&A, 488, 565
Chiang, E., & Youdin, A. N. 2010, AREPS, 38, 493
Clarke, C. J., Gendrin, A., & Sotomayor, M. 2001, MNRAS, 328, 485
Coughlan, C. P., & Gabuzda, D. C. 2013, European Physical Journal Web of Conferences, 61, 7009
Cutri, R. M., Skrutskie, M. F., van Dyk, S., et al. 2003, yCat, 2246, 0
Dong, R., Zhu, Z., Rafikov, R., & Stone, J. 2015, ApJL, 809, L5
Draine, B. T. 2003, ApJ, 598, 1017
Dubrulle, B., Marié, L., Normand, C., et al. 2005, A&A, 429, 1
Dullemond, C., Juhasz, A., Pohl, A., et al. 2015, RADMC3D v0.39 http://www.ita.uni-heidelberg.de/dullemond/software/radmc-3d/
Elia, D., Strafella, F., Campeggio, L., Maiolo, B., & Pezzuto, S. 2005, NewA, 10, 545
Espaillat, C., Muzerolle, J., Najita, J., et al. 2014, in Protostars and Planets VI, ed. H. Beuther et al. (Tucson, AZ: Univ. Arizona Press), 497
Fouchet, L., Gonzalez, J.-F., & Maddison, S. T. 2010, A&A, 518, A16
Fukagawa, M., Tsukagoshi, T., Momose, M., et al. 2013, PASJ, 65, L14
Goodman, J., Narayan, R., & Goldreich, P. 1987, MNRAS, 225, 695
Grady, C. A., Muto, T., Hashimoto, J., et al. 2013, ApJ, 762, 48
Haghighipour, N., & Boss, A. P. 2003, ApJ, 583, 996
Hartmann, L., Calvet, N., Gullbring, E., & D'Alessio, P. 1998, ApJ, 495, 385
Henyey, L. G., & Greenstein, J. L. 1941, ApJ, 93, 70
Høg, E., Fabricius, C., Makarov, V. V., et al. 2000, A&A, 355, L27
Hollenbach, D., Johnstone, D., Lizano, S., & Shu, F. 1994, ApJ, 428, 654
Inaba, S., & Barge, P. 2006, ApJ, 649, 415
Isella, A., Natta, A., Wilner, D., Carpenter, J. M., & Testi, L. 2010, ApJ, 725, 1735
Isella, A., Pérez, L. M., Carpenter, J. M., et al. 2013, ApJ, 775, 30
Isella, A., Tatulli, E., Natta, A., & Testi, L. 2008, A&A, 483, L13
Johansen, A., Andersen, A. C., & Brandenburg, A. 2004, A&A, 417, 361
Klahr, H. H., & Henning, T. 1997, Icar, 128, 213
Lesur, G., & Papaloizou, J. C. B. 2009, A&A, 498, 1
Lesur, G., & Papaloizou, J. C. B. 2010, A&A, 513, A60
Levanda, R., & Leshem, A. 2010, ISPM, 27, 14
Li, A., & Greenberg, J. M. 1997, A&A, 323, 566
Lynden-Bell, D., & Pringle, J. E. 1974, MNRAS, 168, 603
Lyra, W., Johansen, A., Klahr, H., & Piskunov, N. 2008, A&A, 491, L41
Lyra, W., Johansen, A., Klahr, H., & Piskunov, N. 2009, A&A, 493, 1125
Lyra, W., & Lin, M.-K. 2013, ApJ, 775, 17
Lyra, W., & Mac Low, M.-M. 2012, ApJ, 756, 62
Marino, S., Perez, S., & Casassus, S. 2015, ApJL, 798, L44
Meeus, G., Montesinos, B., Mendigutía, I., et al. 2012, A&A, 544, A78
Meheut, H., Keppens, R., Casse, F., & Benz, W. 2012, A&A, 542, A9
Mittal, T., & Chiang, E. 2015, ApJL, 798, L25
Pantin, E., & Starck, J.-L. 1996, A&AS, 118, 575
Pérez, L. M., Isella, A., Carpenter, J. M., & Chandler, C. J. 2014, ApJL, 783, L13
Perryman, M. A. C., Lindegren, L., Kovalevsky, J., et al. 1997, A&A, 323, L49
Pinilla, P., Benisty, M., & Birnstiel, T. 2012, A&A, 545, A81
Pollack, J. B., Hubickyj, O., Bodenheimer, P., et al. 1996, Icarus, 124, 62
Raettig, N., Klahr, H., & Lyra, W. 2015, ApJ, 804, 35
Railton, A. D., & Papaloizou, J. C. B. 2014, MNRAS, 445, 4409
Regály, Z., Juhász, A., Sándor, Z., & Dullemond, C. P. 2012, MNRAS, 419, 1701
Safronov, V. S., & Zvjagina, E. V. 1969, Icar, 10, 109
Surville, C., & Barge, P. 2015, A&A, 579, A100
Tanga, P., Babiano, A., Dubrulle, B., & Provenzale, A. 1996, Icar, 121, 158
Testi, L., Natta, A., Shepherd, D. S., & Wilner, D. J. 2003, A&A, 403, 323
van den Ancker, M. E., de Winter, D., & Tjin A Djie, H. R. E. 1998, A&A, 330, 145
van der Marel, N., van Dishoeck, E. F., Bruderer, S., et al. 2013, Sci, 340, 1199
van Leeuwen, F. 2007, A&A, 474, 653
Warmuth, A., & Mann, G. 2013, A&A, 552, A86
Weidenschilling, S. J. 1977, MNRAS, 180, 57
Whipple, F. L. 1972, in Proc. of the Twenty-First Nobel Symposium, From Plasma to Planet, ed. A. Elvius (New York: Wiley), 211
Zhu, Z., & Stone, J. M. 2014, ApJ, 795, 53